Influence of reflected radiation waves caused by large mode field and large refractive index mismatches on splice loss evaluation between elliptical-hole lattice core holey fibers and conventional fibers

Influence of reflected radiation waves caused by large mode field and large refractive index mismatches on the splice loss evaluation between elliptical-hole lattice core holey fibers and conventional fibers

Masashi Eguchi

Department of Photonics System Technology, Chitose Institute of Science and Technology, Chitose, 066-8655 JAPAN

megu@ieee.org

Yasuhide Tsuji

Division of Information and Electronic Engineering, Graduate School of Engineering, Muroran Institute of Technology, Muroran, 050-8585 JAPAN

y-tsuji@mmm.muroran-it.ac.jp

When the mode field and refractive index mismatches between two spliced fibers are small, the splice loss is generally evaluated by calculating an overlap integral without reflection waves. A single-polarization circular-hole holey fiber with a core consisting of an elliptical-hole lattice (EC-CHF) has a strikingly different mode field caused by elliptical holes in the core region from those of conventional single-mode fibers (SMFs) and, thus, reflected radiation modes may significantly appear in splicing an EC-CHF to conventional SMFs. We study the influence of reflected radiation modes on the splice loss evaluation of optical fibers with large mode field and large refractive index mismatches through numerical analyses using a bidirectional eigenmode propagation method and a three-dimensional finite-element method. © 2012 Optical Society of America

OCIS codes: 060.2310, 060.2400, 060.4005.

1. INTRODUCTION

Novel optical fibers with very different structures from conventional single-mode fibers (SMFs), which are microstructured fibers with complicated cross-sectional structures consisting of a single material with many air holes, referred to as photonic crystal fibers (PCFs) or holey fibers (HFs) [1–3], multicore fibers having a small composite core consisting of multiple coupled small round cores [4,5], and optical nanowires or nanofibers with subwavelength-diameters [6,7], enable unique and adjustable transmission characteristics very different from those of conventional SMFs. Such optical fibers with unconventional structures have particular mode fields compared with conventional SMFs and, thus, the splice losses with conventional SMFs are a crucial issue for their practical implementation.

So far, many theoretical evaluations have been reported on splice losses between optical fibers, including PCFs [8–12]. Splice losses between two different waveguides can be calculated by a mode orthogonality [13–15]. Since when the mode field and refractive index mismatches between two spliced fibers are small, reflections at the interface between them can be neglected, the splice loss can be evaluated by calculating a simple overlap integral based on the mode orthogonality [9–11,16]. Standard refractive-index guiding HFs [1,3], which are formed by an air-hole lattice surrounding a solid central core region, have mode field distributions somewhat different from those of conventional SMFs. However, since the core regions of these HFs are formed

3

by a homogeneous solid medium, their fundamental modes have a Gaussian-like mode field inside the core regions which strongly affect them. Thus, a simple approach using the overlap integral without reflections may also be applied to the splice loss evaluation between such an HF and a conventional SMF. [16, 17]. However, in splicing two fibers with strikingly different mode fields and largely different refractive indices, such as a conventional SMF and an HF having a core including air holes, reflections at the interface may not be neglected. To the best of our knowledge, the influence of reflection waves on evaluating waveguide splice losses has never been reported in detail before.

A novel single-polarization HF [18, 19] and an extremely high birefringent squeezed lattice elliptical-hole HF [20], which have a core consisting of an elliptical-hole lattice, have recently been proposed. Since there are air-silica interfaces in splicing a conventional SMF to these unconventional HFs, reflections in their splicing will be more significant than in splicing a conventional SMF to a standard HF. In Ref. [12], the splice loss between a conventional SMF and a hollow-core photonic-bandgap fiber (PBF) has been evaluated using the overlap integral including a reflected fundamental mode. Hollow-core PBFs have certainly remarkably different structures compared with SMFs, but their fundamental modes have a Gaussian-like mode field in their core regions of high intensity. Therefore, since the mode field mismatch between a hollow-core PBF and an SMF is relatively small, most of the reflection wave seems to consist of the fundamental mode component. On the other hand, a circular-hole

holey fiber with a core consisting of an elliptical-hole lattice (EC-CHF) [18, 19, 21, 22] shown in Fig. 1, which can be easily designed as a single-polarization fiber by using the fundamental space-filling modes [23] of the core and cladding lattices, has a strikingly different mode field caused by elliptical holes in the core region from those of SMFs and, thus, the reflected radiation modes may significantly appear in splicing an EC-CHF to an SMF. In this article, we therefore apply a bidirectional eigenmode propagation (BEP) method and a three-dimensional (3D) finite-element method (FEM) with a perfectly matched layer [21], which can involve reflected radiation modes, to a fiber splice problem between an EC-CHF and an SMF and investigate the influence of reflected radiation modes on the splice loss evaluation between optical fibers with large mode field and large refractive index mismatches by comparing the evaluation based on the overlap integral (not including reflected radiation modes) with the BEP method and FEM analyses. In addition, we test the validity of a simple splice loss evaluation by approximating an EC-CHF with an equivalent step-index (SI) fiber.

Splice losses in a butt joint between two fibers are classified as follows:

- **Mode field mismatch loss**

- **(Lateral) offset loss**

- Tilt loss

- End-separation loss

In the present study, we focus on the mode field mismatch and offset losses between a single-polarization EC-CHF and an SMF. We first provide the fundamentals for evaluating the splice losses between them in Section 2. The influence of neglecting reflected radiation modes on evaluating the splice losses is discussed in Section 3. In Section 4, the splice losses of EC-CHFs are evaluated using the overlap integral method in detail. In Section 5, the directly 3D FEM analysis is applied to calculate the mode field distributions in a spliced fiber consisting of an EC-CHF and an SMF.

2. THEORETICAL FORMULATION FOR SPLICE LOSS EVALUATION

2.A. Overlap Integral Method

When, in splicing between two single-mode waveguides represented by subscripts 1 and 2, the fundamental mode of the waveguide 1 is incident on the interface between the two waveguides, the continuity of electromagnetic fields at the interface provides

$$\boldsymbol{E}_{1t} + c_r \boldsymbol{E}_{1t} + \int_0^\infty c_r(\rho) \boldsymbol{E}_{1t}(\rho) d\rho = c_t \boldsymbol{E}_{2t}$$

$$+ \int_0^\infty c_t(\rho) \boldsymbol{E}_{2t}(\rho) d\rho, \tag{1}$$

$$\boldsymbol{H}_{1t} - c_r \boldsymbol{H}_{1t} - \int_0^\infty c_r(\rho) \boldsymbol{H}_{1t}(\rho) d\rho = c_t \boldsymbol{H}_{2t}$$

$$+ \int_0^\infty c_t(\rho) \boldsymbol{H}_{2t}(\rho) d\rho, \tag{2}$$

where $\boldsymbol{E}_t$ and $\boldsymbol{H}_t$ represent the transverse-electromagnetic field functions of the fundamental mode, $\boldsymbol{E}_t(\rho)$ and $\boldsymbol{H}_t(\rho)$ represent those of the continuous radiation modes,

c_r and c_t are amplitude reflection and transmission coefficients, respectively, of the fundamental mode, and $c_r(\rho)$ and $c_t(\rho)$ are those of the continuous radiation modes. Integrating Eq.(1) $\times \boldsymbol{H}_{2t}$ and $\boldsymbol{E}_{2t} \times$ Eq.(2) over the cross section and applying the mode orthogonality, we obtain

$$(1 + c_r)I_{12} = c_t I_{11}, \tag{3}$$

$$(1 - c_r)I_{21} = c_t I_{22}, \tag{4}$$

with

$$I_{ij} = \int_S (\boldsymbol{E}_{it} \times \boldsymbol{H}_{jt}) \cdot \boldsymbol{i}_z dS, \quad i, j = 1, 2, \tag{5}$$

where only the reflected radiation modes are neglected, $\boldsymbol{i}_z$ is a unit vector in the direction of the waveguide axis, and the integrals extend over the infinite cross section. Transmission coefficient η is, thus, expressed by

$$\eta = c_t^2 \frac{I_{22}}{I_{11}} = \frac{4I_{21}^2 I_{12}^2}{I_{11}I_{22}(I_{21} + I_{12})^2}. \tag{6}$$

It should be noted that a transmitted fundamental mode, transmitted radiation modes, and a reflected fundamental mode are included in Eq. (6), whereas reflected radiation modes are not included; therefore the accuracy of the evaluation based on the overlap integral seems to be somewhat degraded. However, to the best of our knowledge, all reflections at the splice interface are neglected in the splice loss formula based on the overlap integral used in previous reports excepting in Ref. [12].

The transverse electromagnetic field vectors of each waveguide can be obtained by

a two-dimensional (2D) vector FEM (V-FEM) [24] based on curvilinear edge/nodal hybrid elements and, then, the integrals (5) over the splice cross section are numerically calculated. On the other hand, when equivalent SI fiber approximation is valid for two spliced fibers, it will allow us to use a simple splice loss evaluation. In Refs. [21,22], we have demonstrated that when the air hole sizes of an EC-CHF are relatively small, this approximation, in which the core and cladding regions are approximated by media with refractive indices equal to the effective refractive indices of the core and cladding lattice, respectively, is valid for the EC-CHF. Using this approximation, the splice problem of EC-CHF can be replaced by a simple splice problem between two different SI fibers, whose mode fields can be analytically obtained. For weakly guiding fibers, Eq. (6) reduces to the simpler form

$$\eta = \frac{4 n_{\text{eff},1} n_{\text{eff},2} \left[\int_S \phi_1 \phi_2 dS\right]^2}{(n_{\text{eff},1} + n_{\text{eff},2})^2 \int_S \phi_1^2 dS \int_S \phi_2^2 dS}, \tag{7}$$

where $n_{\text{eff},i}$ is the effective index of each fiber mode. In local cylindrical coordinates (r,θ) centered on each fiber, the radial mode field ϕ_i is given by

$$\phi_i = \begin{cases} A J_0(\sqrt{k_0^2 n_{1,i}^2 - n_{\text{eff},i}^2} r) & (r \le a_i) \\ \\ B K_0(\sqrt{n_{\text{eff},i}^2 - k_0^2 n_{2,i}^2} r) & (r > a_i) \end{cases}, \tag{8}$$

$$B = A \frac{J_0(\sqrt{k_0^2 n_{1,i}^2 - n_{\text{eff},i}^2} a_i)}{K_0(\sqrt{n_{\text{eff},i}^2 - k_0^2 n_{2,i}^2} a_i)}, \tag{9}$$

where J_0 and K_0 denote the ordinary Bessel function of the first kind and the modified Bessel function of the second kind, respectively, a_i is the core radius of each fiber, k_0 is the free-space wavenumber, and $n_{1,i}$ and $n_{2,i}$ are the core and cladding indices,

8

respectively. For example, because an equivalent SI fiber for a 1.55 μm zero-dispersion EC-CHF designed in Ref. [19] is weakly guiding, Eq. (7) is available. An overlap-integral corresponding to the numerator of Eq. (7) is approximately obtained by numerically integrating it for the mode field functions ϕ_i of two spliced fibers in the cylindrical coordinate system R and Θ at the splice interface shown in Fig. 2.

2.B.   *Bidirectional Eigenmode Propagation Method*

In a bidirectional eigenmode propagation (BEP) method, first, an optical waveguide is divided into small segments in the propagation direction, and each segment is assumed to be uniform in the propagation direction, as shown in Fig. 3. Next, the electromagnetic fields in each segment are expanded in the eigenmodes in the segment. The expansion coefficients are determined by imposing the boundary condition to the electromagnetic fields in each segment on the interface between adjacent segments. Using the BEP method, we can evaluate the splice losses including reflection waves, because this method involves both forward and backward waves.

2.B.1.   Eigenmode Expansion

In a segment Ω_k in Fig. 3, the electromagnetic fields can be expressed by

$$\boldsymbol{E}_k = \sum_l \boldsymbol{e}_{kl} \left\{ A_{kl} \exp\left[-j\beta_{kl}(z - z_k)\right] \right.$$

$$\left. + \ B_{kl} \exp\left[j\beta_{kl}(z - z_k)\right] \right\}, \tag{10}$$

$$\boldsymbol{H}_k = \sum_l \boldsymbol{h}_{kl} \left\{ A_{kl} \exp\left[-j\beta_{kl}(z - z_k)\right] \right.$$

$$\left. - \ B_{kl} \exp\left[j\beta_{kl}(z - z_k)\right] \right\}, \tag{11}$$

where l is the mode order of eigenmode and $\boldsymbol{e}_{kl}$, $\boldsymbol{h}_{kl}$, and β_{kl} are the electric, magnetic

field vectors, and propagation constant of each eigenmode, respectively. A_{kl} and B_{kl}

represent the amplitudes of forward and backward waves, respectively.

2.B.2.   Transfer Matrix

Imposing the continuity of electromagnetic fields at $z = z_k$, we obtain the following

relations:

$$\sum_l \boldsymbol{e}_{kl}(A_{kl} + B_{kl}) = \sum_l \boldsymbol{e}_{(k+1)l} \left\{ A_{(k+1)l} \exp\left(j\beta_{(k+1)l}d_{k+1}\right) \right.$$

$$\left. + \ B_{(k+1)l} \exp\left(-j\beta_{(k+1)l}d_{k+1}\right) \right\}, \tag{12}$$

$$\sum_l \boldsymbol{h}_{kl}(A_{kl} - B_{kl}) = \sum_l \boldsymbol{h}_{(k+1)l} \left\{ A_{(k+1)l} \exp\left(j\beta_{(k+1)l}d_{k+1}\right) \right.$$

$$\left. - \ B_{(k+1)l} \exp\left(-j\beta_{(k+1)l}d_{k+1}\right) \right\}, \tag{13}$$

$$d_{k+1} = z_{k+1} - z_k. \tag{14}$$

In order to get the relation between A_{kl}, B_{kl} and $A_{(k+1)l}$, $B_{(k+1)l}$, integrating Eq. (12)

$\times \boldsymbol{h}_{ki}^*$ and $\boldsymbol{e}_{ki}^* \times$ Eq. (13) over the cross section and applying the mode orthogonality,

we obtain

$$
\begin{bmatrix} \{A\}_k \\ \{B\}_k \end{bmatrix} = [F]_{k+1} \begin{bmatrix} \{A\}_{k+1} \\ \{B\}_{k+1} \end{bmatrix}
$$

$$
= \begin{bmatrix} [P]_{k+1} & [Q]_{k+1} \\ [R]_{k+1} & [S]_{k+1} \end{bmatrix} \begin{bmatrix} \{A\}_{k+1} \\ \{B\}_{k+1} \end{bmatrix}, \tag{15}
$$

where the (i, l) elements of $[P]_{k+1}$, $[Q]_{k+1}$, $[R]_{k+1}$, and $[S]_{k+1}$ are given respectively

by

$$
P_{(k+1)il} = \frac{1}{2} \left(\frac{f^{(1)}_{kil}}{f^{(0)}_{kii}} + \frac{g^{(1)}_{kil}}{g^{(0)}_{kii}} \right) \exp\left(j\beta_{(k+1)l}d_{k+1}\right), \tag{16}
$$

$$
Q_{(k+1)il} = \frac{1}{2} \left(\frac{f^{(1)}_{kil}}{f^{(0)}_{kii}} - \frac{g^{(1)}_{kil}}{g^{(0)}_{kii}} \right) \exp\left(-j\beta_{(k+1)l}d_{k+1}\right), \tag{17}
$$

$$
R_{(k+1)il} = \frac{1}{2} \left(\frac{f^{(1)}_{kil}}{f^{(0)}_{kii}} - \frac{g^{(1)}_{kil}}{g^{(0)}_{kii}} \right) \exp\left(j\beta_{(k+1)l}d_{k+1}\right), \tag{18}
$$

$$
S_{(k+1)il} = \frac{1}{2} \left(\frac{f^{(1)}_{kil}}{f^{(0)}_{kii}} + \frac{g^{(1)}_{kil}}{g^{(0)}_{kii}} \right) \exp\left(-j\beta_{(k+1)l}d_{k+1}\right), \tag{19}
$$

$$
f^{(\xi)}_{kil} = \int_S (\boldsymbol{e}_{(k+1)l} \times \boldsymbol{h}^*_{ki}) \cdot \boldsymbol{i}_z dS, \tag{20}
$$

$$
g^{(\xi)}_{kil} = \int_S (\boldsymbol{e}^*_{kl} \times \boldsymbol{h}_{(k+1)i}) \cdot \boldsymbol{i}_z dS, \quad \xi = 0, 1. \tag{21}
$$

In this article, in order to calculate the overlap integrals of Eqs. (20) and (21), the

eigenmodes in each segment are calculated using the FEM. Applying Eq. (15) iter-

atively, we can relate the amplitude coefficient vectors at the output interface (at

11

$z = z_N$) to those in the incident interface (at $z = z_0$).

$$
\begin{bmatrix} \{A\}_0 \\ \{B\}_0 \end{bmatrix} = [F] \begin{bmatrix} \{A\}_N \\ \{B\}_N \end{bmatrix} = \begin{bmatrix} [P] & [Q] \\ [R] & [S] \end{bmatrix} \begin{bmatrix} \{A\}_N \\ \{B\}_N \end{bmatrix}, \tag{22}
$$

$$
[F] = \prod_{k=1}^{N} [F]_k. \tag{23}
$$

Since only the transmitted wave propagates in the region outside the output interface,

$\{B\}_N = 0$. Therefore, the transmitted wave vector $\{A\}_N$ and the reflected wave vector

$\{B\}_0$ can be calculated by

$$
\{A\}_N = [P]^{-1} \{A\}_0, \tag{24}
$$

$$
\{B\}_0 = [R]\{A\}_N = [R][P]^{-1}\{A\}_0. \tag{25}
$$

2.C.   Three-Dimensional Finite-Element Method

A 3D FEM would be one of direct approaches to analyze waveguide structures that

are not uniform along the propagation direction. The mode field distribution in a 3D

waveguide is described by the vector wave equation,

$$
\nabla \times ([p]\nabla \times \boldsymbol{\Phi}) - k_0^2 [q] \boldsymbol{\Phi} = 0, \tag{26}
$$

where $\boldsymbol{\Phi}$ represents either the electric field $\sqrt{\varepsilon_0}\boldsymbol{E}$ or the magnetic field $\sqrt{\mu_0}\boldsymbol{H}$ and

$$
[p] = [\mu_r]^{-1}, [q] = [\varepsilon_r] \qquad \text{for} \quad \sqrt{\varepsilon_0}\boldsymbol{E}, \tag{27}
$$

$$
[p] = [\varepsilon_r]^{-1}, [q] = [\mu_r] \qquad \text{for} \quad \sqrt{\mu_0}\boldsymbol{H}. \tag{28}
$$

Here $[\varepsilon_r]$ and $[\mu_r]$ represent a relative permittivity and relative permeability tensors,

respectively. In the 3D FEM analysis, first, a 3D space of interest is divided into a

12

number of tetrahedral elements shown in Fig. 4 and the electromagnetic field vector $\boldsymbol{\Phi}$ in each element is expanded as

$$\boldsymbol{\Phi} = \left(\{U\}^T \boldsymbol{i}_x + \{V\}^T \boldsymbol{i}_y + \{W\}^T \boldsymbol{i}_z\right)\{\Phi_e\} = \{\boldsymbol{N}\}\{\Phi_e\}, \tag{29}$$

where $\{\Phi_e\}$ denotes the tangential field variable vector along the edges for each element, $\{U\}$, $\{V\}$, and $\{W\}$ are the shape function vectors for edge elements, ^{T} symbolizes matrix transpose, and $\boldsymbol{i}_x$, $\boldsymbol{i}_y$, and $\boldsymbol{i}_z$ are, respectively, the unit vectors in the x, y, and z directions.

The entire analysis space is divided into two subspaces Ω_A and Ω_B at an incident interface Γ perpendicular to the z-direction and by applying a Galerkin procedure to Eq. (26) for each subspace, the following simultaneous linear equations are obtained.

$$[P_i]\{\Phi_i\} = \left([K_i] - k_0^2[M_i]\right)\{\Phi_i\} = \{u_i\}, \quad i = A, B, \tag{30}$$

where

$$[K_i] = \sum_{e_i} \iiint_{e_i} (\nabla \times \{\boldsymbol{N}\}) \cdot ([p]\nabla \times \{\boldsymbol{N}^T\}) dV, \tag{31}$$

$$[M_i] = \sum_{e_i} \iiint_{e_i} \{\boldsymbol{N}\} \cdot ([q]\{\boldsymbol{N}^T\}) dV, \tag{32}$$

$$\{u_i\} = \sum_{S_i} \iint_{S_i} \{\boldsymbol{N}\}_{S_i} \cdot \{\boldsymbol{i}_n \times ([p]\nabla \times \boldsymbol{\Phi})\}_{S_i} dS, \tag{33}$$

where S_i represents the surface surrounding the subspace Ω_i including the incident interface Γ, the summations $\sum_{e_i}$ and $\sum_{S_i}$ extend over all different elements and the elements related to S_i, respectively, in each subspace, and the integrals $\iiint_{e_i} dV$ and $\iint_{S_i} dS$ extend over each element volume and over the surface S_i, respectively, in each

subspace. In fact, note that while $\{u_i\}$ should contain not only the surface integrals over the external surface surrounding Ω_i but also ones over each element surface inside Ω_i, in the summation of $\{u_i\}$ ones over each element surface are canceled by the continuity of electromagnetic fields on the element boundaries and, finally, only ones over the external surface S_i remain.

Next, separating $\{\Phi_i\}$ into $\{\Phi_i\}_\Gamma$ at nodes on the incident interface Γ and $\{\Phi_i\}_0$ related to the remaining nodes, we can write Eq. (30) in the form,

$$
\begin{bmatrix} [P_i]_{00} & [P_i]_{0\Gamma} \\ [P_i]_{\Gamma 0} & [P_i]_{\Gamma\Gamma} \end{bmatrix} \begin{bmatrix} \{\Phi_i\}_0 \\ \{\Phi_i\}_\Gamma \end{bmatrix} = \begin{bmatrix} \{u_i\}_0 \\ \{u_i\}_\Gamma \end{bmatrix}. \tag{34}
$$

We can divide the electromagnetic field $\boldsymbol{\Phi}_i$ on the Ω_i side of Γ into the incident field $\boldsymbol{\Phi}_{i,\mathrm{in}}$ to Γ and the scattering wave $\boldsymbol{\Phi}_{i,\mathrm{scat}}$, so that

$$
\boldsymbol{\Phi}_i|_\Gamma = \boldsymbol{\Phi}_{i,\mathrm{in}}|_\Gamma + \boldsymbol{\Phi}_{i,\mathrm{scat}}|_\Gamma. \tag{35}
$$

The continuity of electromagnetic fields on Γ yields

$$
\boldsymbol{i}_n \times (\nabla \times \boldsymbol{\Phi}_{A,\mathrm{scat}})_\Gamma = -\boldsymbol{i}_n \times (\nabla \times \boldsymbol{\Phi}_{B,\mathrm{scat}})_\Gamma, \tag{36}
$$

$$
\boldsymbol{\Phi}_{A,\mathrm{scat}}|_\Gamma = \boldsymbol{\Phi}_{B,\mathrm{scat}}|_\Gamma = \boldsymbol{\Phi}_{\mathrm{scat}}|_\Gamma. \tag{37}
$$

Applying these continuity conditions to the matrix equations Eq. (34) for both sub-

spaces $(i = A, B)$, we finally obtain

$$
\begin{bmatrix}
[P_A]_{00} & [0] & [P_A]_{0\Gamma} \\
[0] & [P_B]_{00} & [P_B]_{0\Gamma} \\
[P_A]_{\Gamma 0} & [P_B]_{\Gamma 0} & [P_A]_{\Gamma\Gamma} + [P_B]_{\Gamma\Gamma}
\end{bmatrix}
\begin{bmatrix}
\{\Phi_A\}_0 \\
\{\Phi_B\}_0 \\
\{\Phi_{\text{scat}}\}_\Gamma
\end{bmatrix}
=
\begin{bmatrix}
\{u_A\}_0 - [P_A]_{0\Gamma}\{\Phi_{A,\text{in}}\}_\Gamma \\
\{u_B\}_0 - [P_B]_{0\Gamma}\{\Phi_{B,in}\}_\Gamma \\
\{u_{A,\text{in}}\}_\Gamma + \{u_{B,\text{in}}\}_\Gamma - [P_A]_{\Gamma\Gamma}\{\Phi_{A,\text{in}}\}_\Gamma - [P_B]_{\Gamma\Gamma}\{\Phi_{B,\text{in}}\}_\Gamma
\end{bmatrix}.
\tag{38}
$$

When the incident fields on both sides of Γ equal to each other:

$$
\Phi_{A,\text{in}}|_\Gamma = \Phi_{B,\text{in}}|_\Gamma = \Phi_{\text{in}}|_\Gamma,
\tag{39}
$$

we can further write Eq. (38) in the simpler form,

$$
\begin{bmatrix}
[P]_{00} & [P]_{0\Gamma} \\
[P]_{\Gamma 0} & [P]_{\Gamma\Gamma}
\end{bmatrix}
\begin{bmatrix}
\{\Phi\}_0 \\
\{\Phi\}_\Gamma
\end{bmatrix}
=
\begin{bmatrix}
\{u\}_0 \\
2\{u_{\text{in}}\}_\Gamma
\end{bmatrix},
\tag{40}
$$

where

$$
[P]_{00} =
\begin{bmatrix}
[P_A]_{00} & [0] \\
[0] & [P_B]_{00}
\end{bmatrix},
\tag{41}
$$

$$
[P]_{0\Gamma} =
\begin{bmatrix}
[P_A]_{0\Gamma} \\
[P_B]_{0\Gamma}
\end{bmatrix},
\tag{42}
$$

$$
[P]_{\Gamma 0} =
\begin{bmatrix}
[P_A]_{\Gamma 0} & [P_B]_{\Gamma 0}
\end{bmatrix},
\tag{43}
$$

$$
[P]_{\Gamma\Gamma} =
\begin{bmatrix}
[P_A]_{\Gamma\Gamma} + [P_B]_{\Gamma\Gamma}
\end{bmatrix}.
\tag{44}
$$

15

Here, $\{u\}_0$ and $\{u_{\text{in}}\}_\Gamma$ are the sum of the surface integrals over the surface surrounding the whole analysis space and the sum of the surface integrals of the incident fields $\mathbf{\Phi}_{\text{in}}|_\Gamma$ over one side of the incident interface, respectively.

An incident field is given for the surface integral over the incident interface Γ in Eq. (33). When the eigenmode field of the incident fiber, which is computed by a 2D V-FEM based on curvilinear edge/nodal hybrid elements, is applied as an incident field, it can be expressed by

$$\mathbf{\Phi}(x, y) = (\{U\}^T \boldsymbol{i}_x + \{V\}^T \boldsymbol{i}_y)\{\Phi_t\}$$

$$+ j\beta\{N\}^T\{\Phi_z'\}\boldsymbol{i}_z, \tag{45}$$

where $\{U\}$ and $\{V\}$, and $\{N\}$ are the shape function vectors for edge and nodal elements, respectively, for 2D edge/nodal elements. Since $\partial/\partial z = -j\beta$ for an eigenmode, substitution of Eq. (45) into Eq. (33) results in

$$\{u_{i,\text{in}}\}_\Gamma = \sum_{\Gamma_i} \iint_{\Gamma_i} \left[\{\boldsymbol{N}\}_{\Gamma_i} \cdot p \left\{ \left(j\beta\Phi_x + \frac{\partial\Phi_z}{\partial x} \right) \boldsymbol{i}_x \right. \right.$$

$$+ \left. \left. \left(j\beta\Phi_y + \frac{\partial\Phi_z}{\partial y} \right) \boldsymbol{i}_y \right\}_{\Gamma_i} \right] dS$$

$$= j\beta \sum_{\Gamma_i} \iint_{\Gamma_i} \left[p \left(\{U\}\{U\}^T + \{V\}\{V\}^T \right) \{\Phi_t\} \right.$$

$$+ \left. p \left(\{U\}\frac{\partial\{N\}^T}{\partial x} + \{V\}\frac{\partial\{N\}^T}{\partial y} \right) \{\Phi_z'\} \right] dS, \tag{46}$$

where the incident fiber is assumed to consist of isotropic media with $[p] = p$. If the outer edge of the analysis space is truncated by a perfectly matched layer boundary

16

condition [25], we have

$$\{u_i\}_0 = \{0\}. \tag{47}$$

3. INFLUENCE OF NEGLECTING REFLECTED RADIATION MODES ON SPLICE LOSS EVALUATIONS OF EC-CHFs

The computational resources required for the overlap integral method based on 2D analysis of fiber cross sections are relatively small compared with those for directly 3D numerical analysis and, thus, the overlap integral method is widely used for the waveguide splice problems. However, since, in the overlap integral method mentioned in Section 2.A, reflected radiation modes at the splice interface are generally neglected, a large mode field and a large refractive index mismatch between two spliced fibers may cause a significant error in the loss prediction using this approach. Thus we investigate the validity of the overlap integral method for evaluating the splice losses between fibers with large mode field and large refractive index mismatches through comparison to other methods: the BEP method and FEM, which can involve reflected radiation modes.

We now consider a butt splice without offset between an EC-CHF and an SMF, as shown in Fig. 5. In this section, numerical results are obtained for a 2D planar waveguide structure, which extends towards infinity in the y direction, with a 2D index profile on the xz-plane cross section of a 3D analysis model shown in Fig. 5 because of computer constraints on the BEP method and 3D FEM analyses for 3D

17

structures, and, thus, the guided mode HE_{11}^{y} of a single-polarization EC-CHF [18,19] corresponds to a TE mode of planar waveguides. The 2D planar waveguide models for two EC-CHF structures with large and small air holes are calculated using the overlap integral method, BEP method, and 2D (xz-plane) FEM. A large air hole EC-CHF consists of 7 elliptical holes in the core region and has a lattice pitch of Λ=1.24 μm, circular hole size of d_C/Λ=0.63, elliptical hole size of d_L/Λ=0.9, and ellipticity of d_L/d_S=2, and its refractive index is assumed to be 1.444. A small air hole EC-CHF, on the other hand, consists of 37 elliptical holes in the core region and has a lattice pitch of Λ=1 μm, circular hole size of d_C/Λ=0.23, elliptical hole size of d_L/Λ=0.4025, and ellipticity of d_L/d_S=3.6. SMFs have core and cladding indices of n_1=1.4479 and n_2=1.444, respectively.

Figures 6 and 7 show the splicing efficiencies η of the large and small air hole EC-CHFs, respectively, for an SMF having a core radius of a_{SMF} at a wavelength of 1.55μm. In Figs. 6 and 7, the solid curve, open circles, and pluses represent the results obtained by the overlap integral method, BEP method, and FEM, respectively. For small air holes, the splicing efficiency calculated with the overlap integral method was observed to be in good agreement with the results using the BEP method and FEM, whereas for large air holes, noticeable differences of approximately 2 % were observed between the overlap integral method and the other two methods.

Figures 8 and 9 show the wave propagations through the interface between three symmetric three-layer slab waveguides with core widths of 1, 3, and 5 μm and a

multilayer planar waveguide, which correspond to SMFs and an EC-CHF, respectively, calculated using the 2D (xz-plane) FEM and correspond to multilayer planar waveguides with thick and thin air layers, respectively, corresponding to large and small air hole EC-CHFs. Significant reflected radiation modes appear in a splice of the multilayer planar waveguide with thick air layers to three-layer slab waveguides compared with that with thin air layers. One can see a large mode field and a large refractive index mismatch between two spliced planar waveguides and, thus, many air-material interfaces between them are likely to emphasize reflections. As seen in Fig. 8, the observed patterns of the reflected radiation modes appear to resemble a multi-slit diffraction pattern resulting from interference among reflection waves from many such air-material interfaces. Figures 10 and 11 show the reflection powers of a large and small air-hole EC-CHFs, respectively, calculated by the BEP method, and the blue-colored solid and red-colored dashed curves represent the reflected fundamental mode and total reflection powers, respectively. From Fig. 10, for the multilayer planar waveguide with thick air layers, the reflected radiation mode power can be predicted to be approximately 10 % of the incident power regardless of the core width of three-layer slab waveguide.

These results indicate that neglecting the reflected radiation modes will lead to an error of a few percent in the evaluation based on the overlap integral method, but although there is a large mode field and a large refractive index mismatch between two spliced fibers, the possible error involved in using the overlap integral method is

19

not as large as expected. On the other hand, strong reflected radiation modes were hardly observed in splicing the multilayer planar waveguide with thin air layers to the three-layer slab waveguides, as seen from Figs. 9 and 11. Thus, we confirmed that the overlap integral method is sufficiently accurate to evaluate the splicing efficiency between a small air hole EC-CHF and an SMF.

4.   SPLICE LOSSES in EC-CHFs

In the above section, the accuracy of the overlap integral method has been proven sufficient even for evaluating the splice losses between fibers with large mode field and large refractive index mismatches. Therefore, in this section, we discuss a detailed evaluation of the splice losses in EC-CHFs by using the overlap integral method and present also a simple splice loss evaluation by approximating a real EC-CHF with an equivalent SI fiber.

4.A.   Mode Field Mismatch Loss

To evaluate the splice loss due to mode field mismatch between an EC-CHF and an SMF, we now consider a butt splice without offset misalignment between them (i.e., $d = 0$ in Fig. 2).

4.A.1.   EC-CHF with Small Air Holes

Figure 12(a) shows the splicing efficiency without offset misalignment between a three-ring EC-CHF with small air holes and an SMF. Here, the single-polarization EC-CHF

20

consisting of 37 elliptical holes in the core region [19] has a lattice pitch of $\Lambda=1$ μm, circular hole size of $d_C/\Lambda=0.23$, elliptical hole size of $d_L/\Lambda=0.4025$, and ellipticity of $d_L/d_S=3.6$, and its refractive index is assumed to be 1.444, as shown in Fig. 1. The SMF has core and cladding indices of $n_1=1.4479$ and $n_2=1.444$, respectively. In Fig. 12, the solid curve represents the splicing efficiency based on Eq. (6) with V-FEM analysis for the real EC-CHF structure and the open circles are the results of Eq. (7) for an equivalent SI fiber corresponding to the real EC-CHF, based on the equivalent SI fiber approximation. The result (open circles) using the simple splice loss evaluation based on the equivalent SI fiber approximation for EC-CHF is in good agreement with that obtained by the accurate V-FEM analysis (solid curve) for the real EC-CHF structure. One can see that a high splicing efficiency of more than approximately 98 % is obtained for a spliced SMF with a core radius larger than that ($a_{\text{equiv}} = 3.5\mu$m) of the equivalent SI fiber for the EC-CHF. The closed circles represent the mode field diameter $2W_M$ of a spliced SMF. The mode field diameter using the Petermann II definition [26] is defined by

$$W_M^2 = 2\frac{\int_0^\infty \phi^2(r)rdr}{\int_0^\infty \left(\frac{d\phi(r)}{dr}\right)^2 rdr}. \tag{48}$$

The mode field diameter falls sharply to a minimum value with an increase in the core radius of SMF and, then, increases slightly. On the other hand, the splicing efficiency rises sharply with an abrupt drop in the mode field diameter of spliced SMF and reaches its maximum efficiency. Figure 12(b) shows the mode field distributions of the

fundamental modes of the EC-CHF and SMFs with a_{SMF} =2, 3, and 4 μm. Comparing

these mode field distributions, one can see that a low splice loss between EC-CHF

and SMF is achieved when the agreement in mode field distribution between them

is good. Figure 13 compares the mode field distributions on the x axis of the small

air hole EC-CHF (red-colored solid curve), the equivalent SI fiber (dashed curve) of

$a_{\mathrm{equiv}} = 3.5\mu$m, and an SMF (blue-colored solid curve) with a core radius of 5 μm.

In this figure, the mode amplitudes are normalized so that all of the mode powers of

these three fibers are equal. The agreement between the EC-CHF and the equivalent

SI fiber is fairly good and we thus consider that the splicing efficiencies of these two

fibers agreed well with each other. We observed that these three fibers have very

similar mode field distributions in their cladding regions.

4.A.2.   EC-CHF with Large Air Holes

Next, we consider a one-ring EC-CHF consisting of 7 large elliptical holes in the

core region, which has a lattice pitch of Λ=1.24 μm, circular hole size of d_C/Λ=0.63,

elliptical hole size of d_L/Λ=0.9, and ellipticity of d_L/d_S=2.0. Its splicing efficiency

with an SMF is shown in Fig. 14(a), where the solid curve and open circles correspond

to the EC-CHF and an equivalent SI fiber with an equivalent core radius of $a_{\mathrm{equiv}} =$

1.86μm, respectively. The closed circles represent the mode field diameter of a spliced

SMF and are the same as those in Fig. 12. The splicing efficiency of the EC-CHF

with large air holes is low compared with that with small air holes demonstrated in

Subsection 4.A.1. This is due to large mode field and large refractive index mismatches between a large air hole EC-CHF and an SMF. The significant peaks in the splicing efficiencies of the EC-CHF and the equivalent SI fiber appear at core radii of $a_{\mathrm{SMF}} =$ 2.8 and 2.5 μm, respectively. Figure 14(b) shows the mode field distributions of the fundamental modes of the EC-CHF and SMFs with $a_{\mathrm{SMF}} =$2, 2.9, and 3.5 μm. We confirmed that, similarly to the results obtained in Subsection 4.A.1, the lowest splice loss is achieved for splicing the EC-CHF to an SMF having the mode field distribution which is in good agreement with that of the EC-CHF. On the other hand, such the peak is only barely visible in the small air hole EC-CHF in Subsection 4.A.1. One can see that, in the equivalent SI fiber, the peak efficiency reaches approximately 100 %, but in the real EC-CHF falls short of it. This is because the mode field distribution of a real large air hole EC-CHF is significantly different from those of SMFs. Figure 15 compares the mode field distributions on the x axis of the large air hole EC-CHF (red-colored solid curve), the equivalent SI fiber (dashed curve) of $a_{\mathrm{equiv}} = 1.86\mu$m, and an SMF (blue-colored solid curve) with a core radius of 5 μm. We observed that the mode fields of the real EC-CHF and the equivalent SI fiber are weakly confined in comparison with that of the SMF. We consider that this reduced the splicing efficiency of the large air hole EC-CHF.

4.B. Offset Loss

In this section, we demonstrate the splicing efficiency in a butt joint with offset misalignment between an EC-CHF and an SMF with a core radius of 5 μm. Of course, the mode field mismatch loss between them is also contained in the calculated splicing efficiency. We first consider the offset loss in splicing the small air hole EC-CHF mentioned in Subsection 4.A.1 to an SMF with $a_{\mathrm{SMF}} = 5\mu$m and show the splicing efficiency in Fig. 16. The solid curves and open circles correspond to the results obtained for the real EC-CHF structure and based on the equivalent SI fiber approximation, respectively. In Fig. 16, the result based on the equivalent SI fiber approximation (open circles) is in very good agreement with that for the real EC-CHF structure (solid curve) and, thus, this will allow us to use the simple splice loss evaluation based on the equivalent SI fiber approximation. One can see that the splicing efficiency gradually reduces with an increase in the offset misalignment and maintains above 85 % even for an offset misalignment being twice the size of the lattice pitch.

Next, we consider the offset loss of large air hole EC-CHF. Figure 17 shows the splicing efficiency with offset misalignment between the large air hole EC-CHF mentioned in Subsection 4.A.2 and the above mentioned SMF. We found that the splicing efficiency of EC-CHF with large air holes is low compared with that with small air holes and declines more gradually with offset misalignment. This is because the mode

24

field of EC-CHF with large air holes is weakly confined in comparison with that with small air holes, as can be seen from Figs. 13 and 15, and, thus, the splicing efficiency is insensitive to offset misalignment. The result based on the equivalent SI fiber approximation shows a similar trend as for the real EC-CHF structure, but is underestimated by approximately 5 %. This is because the mode field of the equivalent SI fiber extends more deeply into the cladding region than those of the real EC-CHF structure and the spliced SMF.

5.   DIRECTLY 3D FEM ANALYSIS OF MODE FIELD DISTRIBU-
TIONS

A beam propagation method (BPM) is very effective for light propagation problems in 3D structures, but mode field distributions involving reflection waves are hard to obtain by this method. In this section, finally, we calculate the mode field distribution in each spliced fiber before and after the fiber splice interface between a large air-hole EC-CHF and an SMF using the 3D FEM. The 3D FEM requires a huge computer memory storage and, thus, we consider an EC-CHF with strong field confinement, which consists of 7 elliptical holes in the core region and has a lattice pitch of Λ=1.24 μm, circular hole size of d_C/Λ=0.65, elliptical hole size of d_L/Λ=0.9, and ellipticity of d_L/d_S=2, and its refractive index is assumed to be 1.444. The core index n_1 and cladding index n_2 of a spliced SMF are assumed to be 1.46 and 1.444, respectively. In the 3D FEM analysis of a 3D structure connecting two different fibers, the element

divisions for both fibers must be matched at the splice interface. Figure 18 shows an element division at the splice interface for an SMF with $a_{\mathrm{SMF}} = 4 \ \mu$m as an example. One can see in Fig. 18 that the division is complicated around the core region.

In order to confirm the accuracy of 3D FEM used here, we first show the splicing efficiency between them in Fig. 19. Errors of approximately 2% between the results obtained by the 3D FEM (blue-colored solid curve) and the overlap integral method (red-colored dashed curve) were observed and this proves the 3D FEM analysis to be valid. The observed errors are approximately equal to those in the results obtained by the overlap integral method for 2D planar waveguide models, mentioned in Section 3. Figures 20(a), 20(b), and 20(c) show the mode field distributions on the xz- and yz-plane cross sections around the splice interfaces between the EC-CHF and three incident SMFs with $a_{\mathrm{SMF}} = 0.5$, 2.0, and 2.5 μm, respectively. One can see from Fig. 20 that the light in the core of SMFs flows into the high-index material regions of the EC-CHF core as if the light is drawn into there, especially for an SMF with $a_{\mathrm{SMF}} = 0.5 \ \mu$m. Figure 21 shows the mode field distributions on fiber cross section before ($z = -0.8\mu$m), at ($z = 0\mu$m), and after ($z = 0.8\mu$m) the splice interface between them. In this figure, the reflected radiation modes in the incident SMFs, which are reflected by many air holes of the EC-CHF, can be clearly observed. On the other hand, the fundamental mode of EC-CHF proves to be formed in the EC-CHF beyond the splice interface and the mode field distribution at the interface appears to be a mixed distribution of those of the SMF and EC-CHF. Thanks to the 3D FEM

26

analysis, we were able to confirm the state of the field distribution of the reflected radiation modes that would occur in a fiber splice between an EC-CHF and an SMF.

6. CONCLUSION

Numerical analyses that can include reflected radiation modes, such as the 3D V-FEM, are required for accurately evaluating the splice losses between non-axisymmetric fibers with large mode field and large refractive index mismatches, but require huge computations. In this article, we investigated the influence of reflected radiation modes on evaluating the splice losses between fibers with strikingly different mode fields and confirmed that even in splicing two fibers like an EC-CHF with a core consisting of an elliptical-hole lattice and an SMF, the reflected radiation modes at the interface between them are relatively small. Thus, we conclude that even though there is a large mode field and a large refractive index mismatch between two spliced fibers, the overlap integral method will provide sufficiently accurate predictions of their splice loss (errors of a few percent). Then, the splice loss property of EC-CHFs was calculated using the overlap integral method with the V-FEM in detail and the simple loss evaluation based on the equivalent SI fiber approximation was also applied to approximately evaluate those. We found that the highest splice efficiency of large air-hole EC-CHFs is reduced by a few percent compared with that in small air-hole EC-CHFs. Our results showed that even though there is a large mode field and a large refractive index mismatch between two spliced fibers, fairly low splice losses can

be achieved when the agreement in mode field distribution between them is good.

References

1. J.C. Knight, T.A. Birks, P.St.J. Russell, and D.M. Atkin, "All-silica single-mode optical fiber with photonic crystal cladding ," Opt. Lett. **21**, 1547 -1549 (1996) [errata: ibid. **22**, 484, (1997).].

2. P.St.J. Russell, "Photonic-crystal fibers ," IEEE/OSA J. Lightwave Technol. **24**, 4729 -4749 (2006).

3. J.C. Knight, "Photonic crystal fibers and fiber lasers ," J. Opt. Soc. Am. B **24**, 1661 -1668 (2007).

4. M.M. Vogel, M. Abdou-Ahmed, A. Voss, and T. Graf "Very-large-mode-area, single-mode multicore fiber ," Opt. Lett. **34**, 2876 -2878 (2009).

5. M.M. Vogel, M. Abdou-Ahmed, A. Voss, and T. Graf "Very-large-mode-area, single-mode multicore fiber: erratum ," Opt. Lett. **35**, 465 -465 (2010).

6. G. Brambilla, F. Xu, and X. Feng, "Fabrication of optical fibre nanowires and their optical and mechanical characterisation ," Electron. Lett. **42**, 517 -519 (2006).

7. G. Brambilla, F. Xu, P. Horak, Y. Jung, F. Koizumi, N.P. Sessions, E. Koukharenko, X. Feng, G.S. Murugan, J.S. Wilkinson, and David J. Richardson, "Optical fiber nanowires and microwires: fabrication and applications ," Adv. Opt. Photon. **1**, 107 -161 (2009).

8. D. Marcuse, "Loss analysis of single-mode fiber splices ," Bell Syst. Tech. J. **56**,

703 -718 (1977).

9. J. Sakai and T. Kimura, "Splice loss evaluation for optical fibers with arbitrary-index profile ," Appl. Opt. **17**, 2848 -2853 (1978).

10. J.P. Meunier and S.I. Hosain, "An efficient model for splice loss evaluation in single-mode graded-index fibers ," IEEE/OSA J. Lightwave Technol. **9**, 1457 -1463 (1991).

11. T. Conese, G. Barbarossa, and M.N. Armenise, "Accurate loss analysis of single-mode fiber/D-fiber splice by vectorial finite-element method ," IEEE Photon. Technol. Lett. **7**, 523 -525 (1995).

12. K.Z. Aghaie, M.J.F. Digonnet, and S. Fan, "Optimization of the splice loss between photonic-bandgap fibers and conventional single-mode fibers ," Opt. Lett. **35**, 1938 -1940 (2010).

13. G. Goubau, "On the excitation of surface waves ," Proc. IRE **40**, 865 -868 (1952).

14. D. Marcuse, *Light Transmission Optics* (Van Nostrand, Reinhold, New York, 1972).

15. J.S. Cook W.L. Mammel, and R.J. Grow, "Effect of misalignments on coupling efficiency of single-mode optical fiber butt joints ," Bell Syst. Tech. J. **52**, 1439 -1448 (1973).

16. Y.L. Hoo, W. Jin, J. Ju, and H.L. Ho, "Loss analysis of single-mode fiber/photonic-crystal fiber splice ," Microwave Opt. Technol. Lett. **40**, 378 -380

(2004).

17. Z. Xu, K. Duan, Z. Liu, Y. Wang, and W. Zhao, "Numerical analysis of splice losses of photonic crystal fibers ," Opt. Communications **282**, 4527 -4531 (2009).

18. M. Eguchi and Y. Tsuji, "Single-mode single-polarization holey fiber using anisotropic fundamental space-filling mode ," Opt. Lett. **32**, 2112 -2114 (2007).

19. M. Eguchi and Y. Tsuji, "Design of single-polarization elliptical-hole core circular-hole holey fibers with zero dispersion at 1.55 μm ," J. Opt. Soc. Am. B **25**, 1690 -1701 (2008).

20. M. Eguchi and Y. Tsuji, "Squeezed lattice elliptical-hole holey fiber with extremely high birefringence ," Opt. Lett. **33**, 1792 -1794 (2008).

21. M. Eguchi and Y. Tsuji, "Bending loss evaluations of holey fibers having a core consisting of an elliptical-hole lattice by various approaches ," IEEE J. Quantum Electron. **46**, 601 -609 (2010).

22. M. Eguchi and Y. Tsuji, "Bending loss of elliptical-hole core circular-hole holey fibers bent in arbitrary bending directions ," Appl. Opt. **49**, 6207 -6212 (2010).

23. T.A. Birks, J.C. Knight, and P.St.J. Russell, "Endlessly single-mode photonic crystal fiber ," Opt. Lett. **22**, 961 -963 (1997).

24. M. Koshiba, S. Maruyama, and K. Hirayama, "A vector finite element method with the high-order mixed-interpolation-type triangular elements for optical waveguiding problems ," IEEE/OSA J. Lightwave Technol. **12**, 495 -502 (1994).

25. J.-P. Berenger, "A perfectly matched layer for the absorption of electromagnetic waves ," J. Comp. Phys. **114**, 185 -200, 1994.

26. K. Petermann, "Constraints for fundamental-mode spot size for broadband dispersion-compensated single-mode fibres ," Electron. Lett. **19**, 712 -714 (1983).

List of figures

BEP method. Blue-colored solid and red-colored dashed curves represent the reflected fundamental mode and total reflection powers, respectively.

Fig.11. (Color online) Reflection power of a small air-hole EC-CHF calculated by the BEP method. Blue-colored solid and red-colored dashed curves represent the reflected fundamental mode and total reflection powers, respectively.

Fig.12. (Color online) Splicing efficiency caused by the mode field mismatch between a small air hole EC-CHF and an SMF. (a) Splicing efficiency against the core radius of SMF. Solid curve and open circles correspond to the EC-CHF and the equivalent SI fiber, respectively. Closed circles represent the mode field diameter (MFD) of SMF. (b) Mode field distributions of the fundamental modes of the EC-CHF and SMFs with $a_{\mathrm{SMF}} =2$, 3, and 4 μm.

Fig.13. (Color online) Mode fields on the x axis of a small air hole EC-CHF (red-colored solid curve), equivalent SI fiber (dashed curve), and SMF (blue-colored solid curve).

Fig.14. (Color online) Splicing efficiency caused by the mode field mismatch between a large air hole EC-CHF and an SMF. (a) Splicing efficiency against the core radius of SMF. Solid curve and open circles correspond to the EC-CHF and the equivalent SI fiber, respectively. Closed circles represent the mode field diameter (MFD) of SMF. (b) Mode field distributions of the fundamental modes of the EC-CHF and SMFs with $a_{\mathrm{SMF}} =2$, 2.9, and 3.5 μm.

Fig.15. (Color online) Mode fields on the x axis of a large air hole EC-CHF (red-

colored solid curve), equivalent SI fiber (dashed curve), and SMF (blue-colored solid curve).

Fig.16. Splicing efficiency caused by butt-joint splice with an offset misalignment between a small air hole EC-CHF and an SMF.

Fig.17. Splicing efficiency caused by butt-joint splice with an offset misalignment between a large air hole EC-CHF and an SMF.

Fig.18. (Color online) Element division at the splice interface for an SMF with $a_{\mathrm{SMF}} = 4$ μm.

Fig.19. (Color online) Splicing efficiency caused by the mode field mismatch between a large air hole EC-CHF and an SMF calculated using the 3D FEM (blue-colored solid curve). Red-colored dashed curve, overlap integral method.

Fig.20. (Color online) Mode fields on the xz- and yz-plane cross sections around the splice interfaces between the EC-CHF and three incident SMFs with $a_{\mathrm{SMF}} = $ (a) 0.5, (b) 2.0, and (c) 2.5 μm.

Fig.21. (Color online) Mode fields before ($z = -0.8\mu$m), at ($z = 0\mu$m), and after ($z = 0.8\mu$m) the fiber splice interface calculated by 3D FEM.

Fig. 1. (Color online) Elliptical-hole core circular-hole holy fiber (EC-CHF).

Fig. 2. (Color online) Calculation of the overlap-integral of the evaluation formula for a butt-joint splice loss.

Fig. 3. (Color online) Schematic drawing of BEP method.

Fig. 4. (Color online) Tetrahedral edge element (blue-colored arrows: edge vector).

Fig. 5. (Color online) Fiber splice between an EC-CHF and an SMF.

Fig. 6. Splicing efficiency caused by the mode field mismatch in the 2D planar waveguide model corresponding to a large air-hole EC-CHF. Solid curve, overlap integral method. Open circles, BEP method. Pluses, xz-plane FEM.

Fig. 7. Splicing efficiency caused by the mode field mismatch in the 2D planar waveguide model corresponding to a small air-hole EC-CHF. Solid curve, overlap integral method. Open circles, BEP method. Pluses, xz-plane FEM.

Fig. 8. (Color online) Wave propagation through the interface between a symmetric three-layer slab waveguide with a core layer width of a_{SMF} and a multilayer planar waveguide with thick air layers. (a) $a_{\mathrm{SMF}} = 1\mu$m. (b) $a_{\mathrm{SMF}} = 3\mu$m. (c) $a_{\mathrm{SMF}} = 5\mu$m.

Fig. 9. (Color online) Wave propagation through the interface between a symmetric three-layer slab waveguide and a multilayer planar waveguide with thin air layers. (a) $a_{SMF} = 1\mu$m. (b) $a_{SMF} = 3\mu$m. (c) $a_{SMF} = 5\mu$m.

Fig. 10. (Color online) Reflection power of a large air-hole EC-CHF calculated by the BEP method. Blue-colored solid and red-colored dashed curves represent the reflected fundamental mode and total reflection powers, respectively.

Fig. 11. (Color online) Reflection power of a small air-hole EC-CHF calculated by the BEP method. Blue-colored solid and red-colored dashed curves represent the reflected fundamental mode and total reflection powers, respectively.
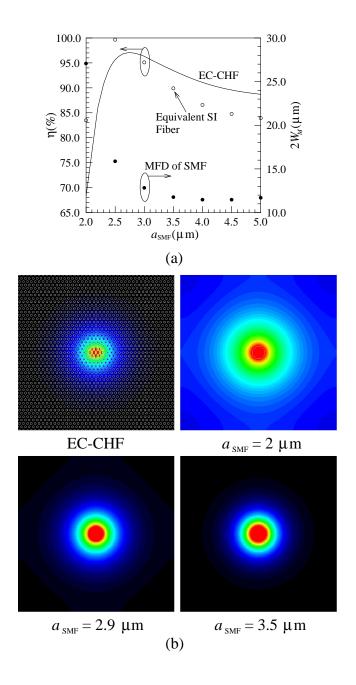
Fig. 12. (Color online) Splicing efficiency caused by the mode field mismatch between a small air hole EC-CHF and an SMF. (a) Splicing efficiency against the core radius of SMF. Solid curve and open circles correspond to the EC-CHF and the equivalent SI fiber, respectively. Closed circles represent the mode field diameter (MFD) of SMF. (b) Mode field distributions of the fundamental modes of the EC-CHF and SMFs with $a_{SMF} =$ 2, 3, and 4 μm.
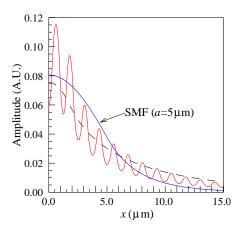
Fig. 13. (Color online) Mode fields on the x axis of a small air hole EC-CHF (red-colored solid curve), equivalent SI fiber (dashed curve), and SMF (blue-colored solid curve).
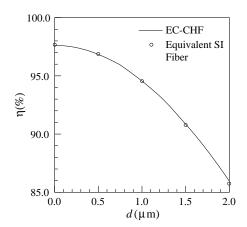
Fig. 14. (Color online) Splicing efficiency caused by the mode field mismatch between a large air hole EC-CHF and an SMF. (a) Splicing efficiency against the core radius of SMF. Solid curve and open circles correspond to the EC-CHF and the equivalent SI fiber, respectively. Closed circles represent the mode field diameter (MFD) of SMF. (b) Mode field distributions of the fundamental modes of the EC-CHF and SMFs with a_{SMF} =2, 2.9, and 3.5 μm.

Fig. 15. (Color online) Mode fields on the x axis of a large air hole EC-CHF (red-colored solid curve), equivalent SI fiber (dashed curve), and SMF (blue-colored solid curve).

Fig. 16. Splicing efficiency caused by butt-joint splice with an offset misalignment between a small air hole EC-CHF and an SMF.
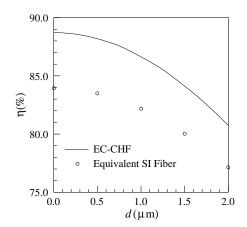
Fig. 17. Splicing efficiency caused by butt-joint splice with an offset misalignment between a large air hole EC-CHF and an SMF.
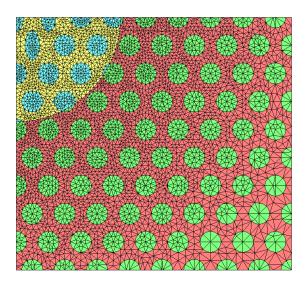
Fig. 18. (Color online) Element division at the splice interface for an SMF with $a_{\mathrm{SMF}} = 4 \ \mu\mathrm{m}$.
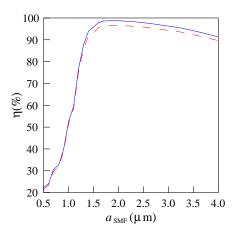
Fig. 19. (Color online) Splicing efficiency caused by the mode field mismatch between a large air hole EC-CHF and an SMF calculated using the 3D FEM (blue-colored solid curve). Red-colored dashed curve, overlap integral method.
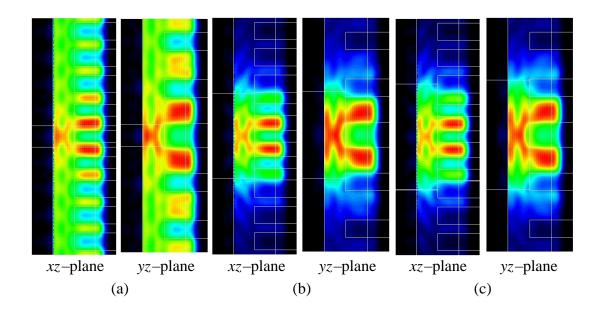
xz–plane yz–plane xz–plane yz–plane xz–plane yz–plane

(a) (b) (c)

Fig. 20. (Color online) Mode fields on the xz- and yz-plane cross sections around the splice interfaces between the EC-CHF and three incident SMFs with $a_{\mathrm{SMF}} =$ (a) 0.5, (b) 2.0, and (c) 2.5 μm.
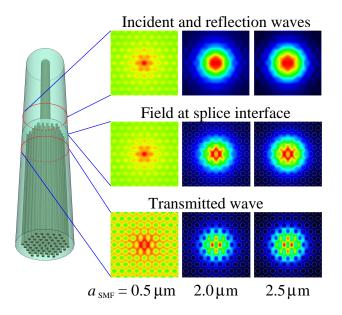
Fig. 21. (Color online) Mode fields before ($z = -0.8\mu$m), at ($z = 0\mu$m), and after ($z = 0.8\mu$m) the fiber splice interface calculated by 3D FEM.